Mass preserving nonrigid registration of CT lung images using cubic B-spline

Youbing Yin
Department of Mechanical and Industrial Engineering, and IIHR–Hydroscience and Engineering, The University of Iowa, Iowa City, Iowa 52242

Eric A. Hoffman[a)]
Department of Radiology, Department of Biomedical Engineering, and Department of Medicine, The University of Iowa, Iowa City, Iowa 52242

Ching-Long Lin[b)]
Department of Mechanical and Industrial Engineering, and IIHR–Hydroscience and Engineering, The University of Iowa, Iowa City, Iowa 52242

(Received 30 December 2008; revised 19 June 2009; accepted for publication 13 July 2009; published 17 August 2009)

The authors propose a nonrigid image registration approach to align two computed-tomography (CT)-derived lung datasets acquired during breath-holds at two inspiratory levels when the image distortion between the two volumes is large. The goal is to derive a three-dimensional warping function that can be used in association with computational fluid dynamics studies. In contrast to the sum of squared intensity difference (SSD), a new similarity criterion, the sum of squared tissue volume difference (SSTVD), is introduced to take into account changes in reconstructed Hounsfield units (scaled attenuation coefficient, HU) with inflation. This new criterion aims to minimize the local tissue volume difference within the lungs between matched regions, thus preserving the tissue mass of the lungs if the tissue density is assumed to be relatively constant. The local tissue volume difference is contributed by two factors: Change in the regional volume due to the deformation and change in the fractional tissue content in a region due to inflation. The change in the regional volume is calculated from the Jacobian value derived from the warping function and the change in the fractional tissue content is estimated from reconstructed HU based on quantitative CT measures. A composite of multilevel B-spline is adopted to deform images and a sufficient condition is imposed to ensure a one-to-one mapping even for a registration pair with large volume difference. Parameters of the transformation model are optimized by a limited-memory quasi-Newton minimization approach in a multiresolution framework. To evaluate the effectiveness of the new similarity measure, the authors performed registrations for six lung volume pairs. Over 100 annotated landmarks located at vessel bifurcations were generated using a semiautomatic system. The results show that the SSTVD method yields smaller average landmark errors than the SSD method across all six registration pairs.
[DOI: 10.1118/1.3193526]

Key words: pulmonary CT, nonrigid registration, large deformation, quantitative CT, B-spline

I. INTRODUCTION

Image registration is a process of determining an optimal spatial mapping that matches images collected at different times or using different imaging modalities.[1] It is becoming a key tool in medical image analysis as one seeks to link images across modalities, across time, or between lung volumes in the use of pulmonary investigations. Registrations of volumetric lung datasets have been applied in establishing lung atlases,[2] segmenting lungs with pathology,[3] linking four-dimensional lung datasets,[4] and tracking the motion of lung tissues.[5–7] There is an important additional motivation to register datasets acquired in one study, whereby the subject is imaged at full inspiration [total lung capacity (TLC)] and at end expiration [functional residual capacity (FRC) or residual volume (RV)]. TLC provides information related to airway and parenchyma structure, while FRC or RV provides information related to air trapping.

A registration algorithm usually consists of three main components:[1] A transformation model, a similarity measure, and an optimization step. The transformation model specifies the spatial mapping of corresponding points between two images. The similarity measure defines how well those two images match and it provides a quantitative criterion for an optimization step to optimize the parameters of a transformation model. According to similarity measures, registration techniques can be divided into feature-based approaches and intensity-based approaches. In the feature-based approach, pairs of corresponding anatomical features, including designated landmarks, contours, and surfaces, are used to define the transformation from one image to the other. Although several groups applied feature-based registrations to lung datasets,[2,8,9] two main difficulties limit its wide application. First, identification of the corresponding features in the images to be registered is a difficult and time-consuming task.

Second, good alignment of features does not guarantee a good correspondence for all lung regions since lung motion is nonrigid. Alternatively, intensity-based registration uses mathematical or statistical criteria from intensity patterns of images to define similarity measures. A common similarity measure used in registrations of computed tomography (CT) lung images is the sum of squared intensity difference (SSD).[2,4–6,10–13] The assumption of SSD is that the corresponding points in both images have the same intensity. The assumption is also implied in the intensity-based registration using optical flow, another common method used to register lung images.[7,14–17] However, this assumption is not valid for the lung which changes voxel intensity due to changes in densities associated with inflation. In addition, normalized correlation[9,18] and mutual information (MI)[19–21] have been used in registering CT lung images. Although these criteria are insensitive to changes in the voxel intensity, they are based on global statistical models of the intensity relationships between voxels in the two images. Since changes in the voxel intensity vary from apex to base and ventral to dorsal, a global model may not be appropriate to capture the nonuniform expansions of the lung. Recently, Sarrut *et al.*[4] proposed *a priori* step to take into account changes in the voxel intensity by artificially adjusting voxel intensity in one image according to the intensity in the other. Although it is only a preprocessing step, their results show an improved registration. This work suggested the importance of taking into account such intensity changes when registering CT lung images.

The reconstructed Hounsfield units (HU) of CT lung images can be used to estimate the amount of air or tissue in each voxel.[22,23] It is assumed that the HU of lung is primarily contributed by two components: Tissue (parenchyma plus blood) and air. Any unit of lung may be considered a linear combination of these two compartments. Thus, the fractional air and tissue contents in a region can be estimated from the HU. Based on this theory, Guerrero *et al.*[7] estimated changes in the regional air content using an intensity-based registration method between two volumetric CT datasets. In addition, this technique was also used by Sarrut *et al.*[4] to link four-dimensional lung datasets. In their work, registration was first done between two inhale and exhale breath-hold CT scans to get the deformation field. The voxel intensity in an intermediate artificial CT image was then estimated from the Jacobian value of the deformation based on the assumption that the mass of tissue between matched regions is constant.

The Jacobian value of the deformation reflects the local contraction or expansion. A Jacobian value of 1 corresponds to no expansion or contraction. It is greater than 1 if there is local expansion and less than 1 if there is local contraction. It is negative if local folding of the deformation exists. The Jacobian value has been used previously in nonrigid image registration. Christensen and Johnson[24] used the Jacobian value to check for folding of the deformation. They monitored the Jacobian value during their consistent image registration to ensure a one-to-one transformation. Rohlfing *et al.*[25] penalized the deviations of the Jacobian value from 1 to develop a volume-preserving nonrigid registration algorithm. The Jacobian value is also used to estimate the local lung tissue contraction or expansion once the deformation field is obtained from the registrations.[5,6]

In this work, we propose a nonrigid image registration method to align two CT lung datasets acquired during breath-hold at two different lung volumes in the same scanning session or over short periods of time. In order to take into account changes in the voxel intensity with inflation, we introduce the sum of squared tissue volume difference (SSTVD) as the similarity criterion. In contrast to previous similarity criteria, SSTVD is based on quantitative CT measures and aims to minimize the local tissue volume (TV) difference within lungs between matched regions. The performance of the new similarity measure is evaluated using six pairs of CT volumetric datasets acquired near TLC and FRC.

II. METHODS

Given two images I_f and I_r, referred to as the floating and reference images, the goal of the registration is to determine a spatial transformation that can match the two images. We assume that $I_f(\mathbf{x})$ and $I_r(\mathbf{x})$ are continuous functions of intensity values at the position $\mathbf{x}$, with $\mathbf{x}=(x,y,z)$, for the floating and reference images, respectively.

II.A. Transformation model

Lung motion is too complicated to be captured by a simple rigid or affine transformation and nonrigid transformation is required. One of the most common nonrigid transformation models is the free-form deformation (FFD) based on cubic B-spline.[26,27] Compared to other transformation models, B-spline-based FFD is locally controlled and, thus, it is computationally efficient even for a large number of control nodes.

Let Φ denote a $n_x \times n_y \times n_z$ uniform grid with $\phi_{i,j,k}$ as the displacement of the ijkth control node. The spacings between the control grids in the x, y, and z directions are denoted by δ_x, δ_y, and δ_z, respectively. The transformation function $T(\mathbf{x};\phi)$ is defined in terms of control nodes as

$$T(\mathbf{x};\phi) = \mathbf{x} + \sum_{l=0}^{3}\sum_{m=0}^{3}\sum_{n=0}^{3} B_l(u)B_m(v)B_n(w)\phi_{i+l,j+m,k+n}, \quad (1)$$

where $i=\lfloor x/\delta_x \rfloor - 1$, $j=\lfloor y/\delta_y \rfloor - 1$, $k=\lfloor z/\delta_z \rfloor - 1$, $u=x/\delta_x-(i+1)$, $v=y/\delta_y-(j+1)$, and $w=z/\delta_z-(k+1)$. Functions B_0 through B_3 are basis functions of cubic B-spline and are defined as follows:

$$B_0(t) = (-t^3+3t^2-3t+1)/6,$$

$$B_1(t) = (3t^3-6t^2+4)/6,$$

$$B_2(t) = (-3t^3+3t^2+3t+1)/6,$$

$$B_3(t) = t^3/6, \quad (2)$$

where $0 \leqslant t < 1$. These basis functions have two important mathematical properties. First, they have a limited support,

which allows efficient computation of the transformation function. Second, they are C^2 continuous, which allows the analytical computation of first-order derivatives of the transformation function. The second property ensures efficient computation and minimization of the new similarity measure described below, which is based on the first-order derivatives.

Since displacements of control nodes act as parameters of the transformation function, the ability of FFD to capture nonrigid deformation depends on the resolution of the control grid. A coarse control grid allows for modeling global nonrigid deformations, while a fine control grid allows for modeling highly local deformations.

The basic FFD algorithm described above may cause folding of the deformation field, leading to negative Jacobian values. The folding could happen in two ways. First, it happens when the B-spline grid contains a self-intersection. Second, the folding may also happen locally within a control block even if the B-spline grid is not self-intersecting (see an example presented in Ref. 28). To ensure a one-to-one mapping, namely, to avoid the folding of the deformation field, Choi and Lee[29] proposed a sufficient condition for three-dimensional cubic B-spline transformation. According to their analysis, a transformation function is locally invertible over the entire domain if components of the displacement of each node in the x, y, and z directions satisfy that $\phi_x < \delta_x/K$, $\phi_y < \delta_y/K$, and $\phi_z < \delta_z/K$, where K is a constant and is approximately 2.479 472 335. With this condition, a point can be deformed at most $(\delta_x/K, \delta_y/K, \delta_z/K)$ if and only if all $4\times4\times4$ surrounding control nodes are displaced by $(\delta_x/K, \delta_y/K, \delta_z/K)$. From this view, a control grid with large spacing is required to model large global deformations for a TLC-FRC registration pair. However, as we discussed above, a fine control grid is required to capture the highly local deformation. To overcome the conflicting requirements of coarse and fine control grids for global and local deformations, respectively, a multilevel B-spline technique[30,31] is adopted in this work.

In the multilevel B-spline algorithm, a hierarchy of control grids, $\Phi_0, \Phi_1, \ldots, \Phi_n$, is used to derive a sequence of transformations with the FFD manipulation described above. The algorithm starts with the coarsest control grid Φ_0. A smooth and one-to-one transformation can be obtained by a FFD manipulation with the displacement constraints. This transformation only has the ability to capture the global motion of lungs. The local motion is then progressively handled by the subsequent transformations with finer control grids. Given $T_0, T_1, \ldots, T_n$ as the sequence of transformations, the final transformation is defined by a composite operation

$$T = T_n \circ T_{n-1} \circ \cdots \circ T_0. \tag{3}$$

To implement the composite operation, we introduce a warping image ϖ, which is a discretized version of the transformation function. The value of each voxel is equal to the physical coordinates of the transformed point of that voxel. Given a voxel $\mathbf{p}$ and its corresponding physical coordinates $\mathbf{x}_0$, the value at $\mathbf{p}$ in the warping image is initially equal to $\mathbf{x}_0$ and then sequentially equal to the transformed point of $\mathbf{x}_0$ after the sequence of transformations. Thus, the composite operation is simplified as a recursive algorithm: $\varpi \leftarrow T_i(\varpi)$.

Since the composition operation will not change the property of invertibility of the transformation, we can get a final one-to-one mapping by imposing the displacement constraints for each FFD manipulation. In addition, as demonstrated in Ref. 31, the multilevel B-spline technique may sufficiently achieve a smooth deformation.

II.B. Cost function

Intensity-based registration tries to match intensity patterns in each image by using mathematical or statistical criteria, also referred to as cost functions. A common cost function is SSD, which is defined as

$$\mathrm{SSD}(\phi) = \sum_{\mathbf{x}\in\Omega} [I_r(\mathbf{x}) - I_f(T^c(\mathbf{x};\phi))]^2. \tag{4}$$

It is noted that T^c is used here to distinguish it from T in Sec. II A since the multilevel B-spline technique is adopted. Given a transformation level i, $T^c(\mathbf{x};\phi)$ is a compound function defined by

$$T^c(\mathbf{x};\phi) = T_i(\varpi(\mathbf{x});\phi), \tag{5}$$

where $T_i(\mathbf{x};\phi)$ is the transformation function at the current level and $\varpi(\mathbf{x})$ is the warping image obtained at the previous level.

The assumption of SSD is that voxel intensities are the same for corresponding points in both reference and floating images. However, this assumption is not valid for the lung which changes voxel intensity with inflation.

We can assume that the HU of lung is primarily contributed by two components: Tissue, which includes parenchyma plus blood, with approximately 55 HU, and air with −1000 HU.[22] Any unit of lung may be considered a linear combination of these two compartments. Let $\nu(\mathbf{x})$ denote the volume of a voxel at position $\mathbf{x}$. The volume of tissue in that voxel can be estimated as

$$V(\mathbf{x}) = \nu(\mathbf{x})\frac{I(\mathbf{x}) + 1000}{1000 + 55} = \nu(\mathbf{x})\tilde{I}(\mathbf{x}), \tag{6}$$

where $\tilde{I}$ is introduced for notational simplicity.

Similarly, the air volume (AV) can be estimated as

$$V'(\mathbf{x}) = \nu(\mathbf{x})\frac{55 - I(\mathbf{x})}{1000 + 55}. \tag{7}$$

Based on this technique, we define a new cost function as the sum of squared local tissue volume difference,

$$E(\phi) = \sum_{\mathbf{x}\in\Omega} [V_r(\mathbf{x}) - V_f(T^c(\mathbf{x};\phi))]^2, \tag{8}$$

where $V_r(\mathbf{x})$ and $V_f(\mathbf{x})$ are tissue volumes in a voxel in the reference image and its corresponding region in the floating image, respectively. Ω denotes the overlap lung regions between the two images.

This new similarity measure is based on the assumption that the tissue (parenchyma plus blood) volume of the lungs is preserved during respiration/static lung volume changes.

TABLE I. The TLV, AV, and TV for all six registration pairs are estimated from the HU based on quantitative CT measures. The percentage change in the tissue volume is also listed for reference. The unit for volumes is liter (l).

Registration pair	Volume	TLC (l)	FRC (l)	Difference (l)	Percentage change |TLC−FRC|/TLC (%)
	TLV	5.31	2.91	2.40	
A	AV	4.62	2.17	2.45	
	TV	0.69	0.74	−0.05	7.2
	TLV	5.11	2.68	2.43	
B	AV	4.51	2.07	2.44	
	TV	0.60	0.61	−0.01	1.7
	TLV	5.94	3.40	2.54	
C	AV	5.23	2.67	2.56	
	TV	0.71	0.73	−0.02	2.8
	TLV	6.41	3.20	3.21	
D	AV	5.58	2.33	3.25	
	TV	0.83	0.87	−0.04	4.8
	TLV	7.18	3.76	3.42	
E	AV	6.31	2.87	3.44	
	TV	0.87	0.89	−0.02	2.3
	TLV	7.28	3.37	3.91	
F	AV	6.41	2.52	3.89	
	TV	0.87	0.85	0.02	2.3
Overall					3.5

We recognize that the tissue volume changes slightly due to pulmonary blood volume changes with lung inflation, but this assumption we make have been proven reasonable since volume change of "tissue" is small and such changes are much smaller than those of air (see Table I for changes in tissue and air volumes between TLC and FRC for all six pairs of datasets used in this work). In addition, the assumption used here has been successfully used in estimating regional specific volume[32] and linking four-dimensional lung datasets.[4] Although changes in the tissue volume due to blood volume changes are taken into consideration by a correction step,[7] such small change appears to be of minimal consequence to our registration process, taking into account the considerable improvement shown in registrations using our new method.

By substituting Eq. (6), Eq. (8) is recast as

$$E(\phi) = \sum_{\mathbf{x}\in\Omega} [\nu_r(\mathbf{x})\tilde{I}_r(\mathbf{x}) - \nu_f(T^c(\mathbf{x};\phi))\tilde{I}_f(T^c(\mathbf{x};\phi))]^2. \quad (9)$$

Given a transformation function, I_f can be interpolated from the floating image using a linear interpolation and ν_f can be calculated from the Jacobian value of the deformation by

$$\nu_f(T^c(\mathbf{x};\phi)) = J(\mathbf{x};\phi)\nu_r(\mathbf{x}), \quad (10)$$

where $J(\mathbf{x};\phi)$ is the Jacobian value and it is defined as the determinant of derivative matrix of the deformation

$$J(\mathbf{x};\phi) = \det(\mathbf{D}) \quad \text{with } \mathbf{D} = \begin{pmatrix} \frac{\partial T_x^c}{\partial x} & \frac{\partial T_x^c}{\partial y} & \frac{\partial T_x^c}{\partial z} \\ \frac{\partial T_y^c}{\partial x} & \frac{\partial T_y^c}{\partial y} & \frac{\partial T_y^c}{\partial z} \\ \frac{\partial T_z^c}{\partial x} & \frac{\partial T_z^c}{\partial y} & \frac{\partial T_z^c}{\partial z} \end{pmatrix}. \quad (11)$$

It is noted that the Jacobian value in Eq. (10) must be positive. This condition is satisfied if the transformation is invertible, which is ensured by the combination of the multilevel B-spline technique and displacement constraints in this work.

Thus, the final form of the new cost function reads as

$$E(\phi) = \sum_{\mathbf{x}\in\Omega} \{\nu_r(\mathbf{x})[\tilde{I}_r(\mathbf{x}) - \tilde{I}_f(T^c(\mathbf{x};\phi))J(\mathbf{x};\phi)]\}^2. \quad (12)$$

Calculation of the gradient of the cost function is necessary for its efficient and robust minimization. For a given transformation variable ϕ, the gradient of cost function is calculated by

$$\frac{\partial E}{\partial \phi} = 2\sum_{\mathbf{x}\in\Omega} [\nu_r(\mathbf{x})]^2 C\frac{\partial C}{\partial \phi}, \quad (13)$$

where C is introduced for notational simplicity. C and its derivative with respect to ϕ are given as

$$C = \tilde{I}_f(T^c(\mathbf{x};\phi))J(\mathbf{x};\phi) - \tilde{I}_r(\mathbf{x}),$$

$$\frac{\partial C}{\partial \phi} = \tilde{I}_f(T^c(\mathbf{x};\phi))\frac{\partial J(\mathbf{x};\phi)}{\partial \phi} + \frac{J(\mathbf{x};\phi)}{1055}\frac{\partial I_f(T^c(\mathbf{x};\phi))}{\partial T^c}\frac{\partial T^c(\mathbf{x};\phi)}{\partial \phi}, \quad (14)$$

where $\partial I_f/\partial T^c$ is the intensity gradient of the floating image. In contrast to SSD, two more terms, the Jacobian value and its derivative with respect to transformation variables, are required. According to Eq. (5), the derivative matrix $\mathbf{D}$ in Eq. (11) can be expanded as the product of two derivative matrices

$$\mathbf{D} = \mathbf{D}^T\mathbf{D}^{\varpi}, \quad (15)$$

where $\mathbf{D}^T$ and $\mathbf{D}^{\varpi}$ denote the derivative matrices of the transformation $T_i(\mathbf{x};\phi)$ and the warping image $\varpi(\mathbf{x})$, respectively. They are defined as follows:

$$\mathbf{D}^T = \begin{pmatrix} \frac{\partial T_{ix}}{\partial x} & \frac{\partial T_{ix}}{\partial y} & \frac{\partial T_{ix}}{\partial z} \\ \frac{\partial T_{iy}}{\partial x} & \frac{\partial T_{iy}}{\partial y} & \frac{\partial T_{iy}}{\partial z} \\ \frac{\partial T_{iz}}{\partial x} & \frac{\partial T_{iz}}{\partial y} & \frac{\partial T_{iz}}{\partial z} \end{pmatrix} \quad \text{and}$$

$$\mathbf{D}^{\varpi} = \begin{pmatrix} \frac{\partial \varpi_x}{\partial x} & \frac{\partial \varpi_x}{\partial y} & \frac{\partial \varpi_x}{\partial z} \\ \frac{\partial \varpi_y}{\partial x} & \frac{\partial \varpi_y}{\partial y} & \frac{\partial \varpi_y}{\partial z} \\ \frac{\partial \varpi_z}{\partial x} & \frac{\partial \varpi_z}{\partial y} & \frac{\partial \varpi_z}{\partial z} \end{pmatrix}. \quad (16)$$

The derivatives of ϖ at a voxel can be derived from its neighbors by using central-difference approximation. For example, $\partial \varpi_x/\partial x = (\varpi_x^+ - \varpi_x^-)/(2\Delta x)$, where superscripts + and − denote the two neighbors of the current voxel in the x direction and Δx is the spacing of the warping image in that direction. In addition, since the cubic B-spline transform is the tensor product of independent one-dimensional functions, the entries of $\mathbf{D}^T$ can be analytically calculated. For example, the derivative of its x component with respect to x is given as

$$\frac{\partial T_{ix}(\mathbf{x};\phi)}{\partial x} = 1 + \frac{1}{\delta_x}\sum_{l=0}^{3}\sum_{m=0}^{3}\sum_{n=0}^{3}\frac{dB_l(u)}{du}B_m(v)B_n(w)\phi_{i+1,j+m,k+n}. \quad (17)$$

The remaining derivatives have an analogous form. Computation of these derivatives is very similar to computing T_i itself with differences that basic functions $B_{0,1,2,3}$ are replaced by their respective derivatives, which are computed as follows:

$$dB_0(t)/dt = (-t^2 + 2t - 1)/2,$$

$$dB_1(t)/dt = (3t^2 - 4t)/2,$$

$$dB_2(t)/dt = (-3t^2 + 2t + 1)/2,$$

$$dB_3(t)/dt = t^2/2. \quad (18)$$

The final terms to discuss from Eq. (14) are derivatives of both the transformation function and the Jacobian value with respect to transformation parameters: $\partial T^c/\partial\phi$ and $\partial J/\partial\phi$. Since ϖ is not a function of ϕ at the current FFD level, both terms are only contributed by T_i. Equations (1), (11), and (17) show that T^c and J have a linear relationship with ϕ. Thus, it is straightforward to compute those two terms: $\partial T^c/\partial\phi$ and $\partial J/\partial\phi$.

II.C. Optimization

An efficient and robust optimization algorithm is required to minimize the cost function by adjusting transformation parameters. Similar to Ref. 33, a limited-memory quasi-Newton minimization method with bounds on the variables (L-BFGS-B)[34] is adopted considering its two advantages. First, it is well suited to handle the high dimensionality of parameter space. Second, it allows bound constraints on the independent variables, making it easy to implement the displacement constraints for a one-to-one mapping discussed in Sec. II A. The parameters given in Ref. 34 are used here.

Multiresolution strategy helps improve the computational efficiency and avoid some local minima. In addition to hierarchical transformation models, multiresolution strategy is also used on images. A pair of image pyramids is built with sequences of gradually reduced resolution images for both the floating and reference images. Here, we use three different levels in both the image pyramids and the hierarchy transformation models. The whole registration is composed of six levels and starts with the coarsest versions of both images and control grid. The images and control grids are then alternatively refined until the finest versions. On each level, optimization is used to minimize the cost function and the displacement constraint is imposed to ensure a one-to-one mapping. The warping image is calculated once the convergence criterion is reached. The warping image is then propagated to the next finer level and is used as a starting transformation at that level. It is noted that upsampling of the warping image is required if the image resolution level changes. The basic idea of the multiresolution strategy is illustrated in Fig. 1.

III. EXPERIMENTS AND RESULTS

III.A. Image data

Datasets from six normal human subjects were used in this study to evaluate the performance of the proposed similarity measure. The subjects were examined under a protocol approved by the University of Iowa's Institutional Review Board. Two volumetric scans were acquired with a Siemens Sensation 64 multidetector row CT scanner (Forchheim, Ger-

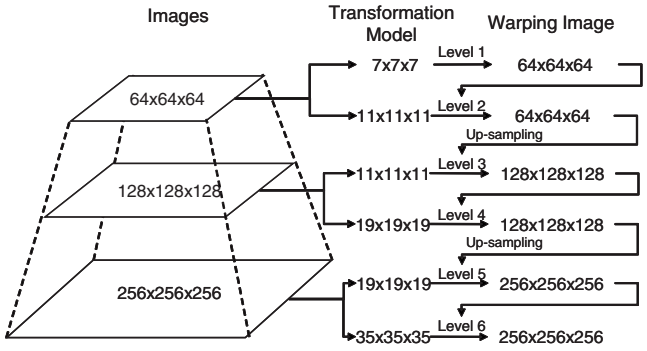

FIG. 1. Framework of the multiresolution strategy.

many) during breath-holds near FRC and TLC in the same scanning session for each subject. Each volumetric dataset contains 550–760 image sections with a section spacing from 0.5 to 0.7 mm and a reconstruction matrix of 512 $\times$512 pixels. In-plane pixel spatial resolution is approximately 0.6×0.6 mm^2. For each dataset, an automatic lung segmentation is performed using the algorithm of Hu *et al.*[35] Experimental studies using human lung CT images have shown that this segmentation algorithm can accurately extract the lung with a root mean square difference between the computer and human analysis of 0.8 voxels and the computational time is 2–3 min on a PC workstation with 300 MHz.[35] Once the lung is extracted, we can estimate the total lung volume (TLV), tissue volume, and air volume, among which the total lung volume is the sum of voxel volumes in the lungs, tissue, and air volume can be estimated from HU using Eqs. (6) and (7). Table I lists these volumes for all datasets. We can find that changes in the tissue volume between TLC and FRC are small for all six registration pairs with an average percentage change of 3.5%. Thus, it is reasonable to assume that the tissue volume is preserved.

III.B. Experimental setup

Given a registration pair, the dataset with the smaller lung volume is taken as the floating image and the one with the larger lung volume is the reference image. Both reference and floating images are first downsampled by a factor of 2 in each dimension, so eight times less voxels, in order to reduce the computational time. The downsampled images are then registered in the multiresolution framework shown in Fig. 1. Once the registration is done, the warped image is upsampled so that it has the same size as the reference image.

In order to evaluate the new similarity measure, we perform registrations with both SSD and SSTVD for comparison. The cost function for the SSD method is evaluated by Eq. (4), whereas for the SSTVD method it is computed by Eq. (12). Lung segmentations of reference and floating images are used as masks for both methods. The mask of the floating image is then dilated by 5×5 voxels in order to improve the matching at lung boundaries. The potential influence of the segmentation on registration results is yet to be investigated. However, we expect that the influence might be small by considering the accuracy of segmentation as discussed previously and that the lung boundary has an obvious contrast with high value of tissue volume for the body and low value inside the lung.

III.C. Results

Landmarks located at vessel bifurcations are used to evaluate registration accuracy. A semiautomatic landmark annotating system[36] is used to guide the observer to generate the corresponding landmarks in TLC and FRC images. Each registration pair has 120-210 landmarks and approximately 20–40 are located in each lobe. Figure 2 shows an example of the landmark locations.

A linear mixed model analysis was used to compare mean landmark error of the SSTVD method with the SSD method and further with the MI method (see the description in the last paragraph in this section). The fixed effects of the model were method (SSTVD, SSD, and MI), initial distance s ($s<20$ mm, $20\leqslant s<40$ mm, $40\leqslant s<60$ mm, $s\geqslant60$ mm), and method $\times$ distance interaction, with subject as the random effect. To satisfy the assumption of normal distribution for the

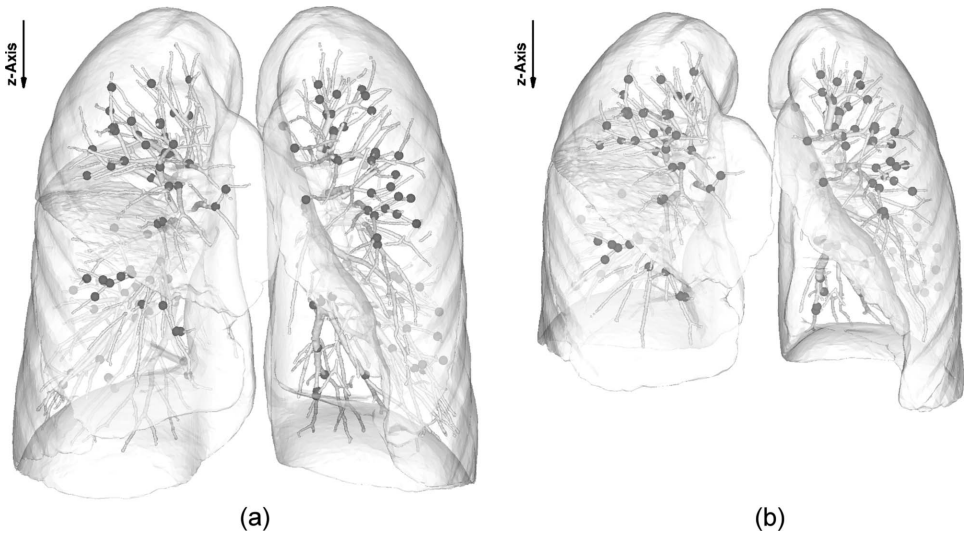

FIG. 2. Locations of the landmarks (marked by spheres) at (a) TLC and (b) FRC for registration pair A. Surface rendering of five lobes and major vessel branches is shown for reference.

TABLE II. Statistical comparison of landmark errors between the SSTVD method, the SSD method, and the MI method for all six registration pairs.

s (mm)	SSTVD (mm)	SSD (mm)	MI (mm)	SSTVD vs SSD		SSTVD vs MI	
				SSTVD/SSD	p value[a]	SSTVD/MI	p value[a]
$s<20$	0.56 ± 0.04	1.84 ± 0.76	0.54 ± 0.07	0.31 ± 0.13	0.243	1.04 ± 0.15	>0.99
$20\leqslant s<40$	0.76 ± 0.06	2.90 ± 1.20	0.70 ± 0.09	0.26 ± 0.11	0.151	1.08 ± 0.16	>0.99
$40\leqslant s<60$	0.81 ± 0.07	4.66 ± 1.94	0.92 ± 0.12	0.17 ± 0.07	0.050	0.88 ± 0.14	>0.99
$s\geqslant60$	1.90 ± 0.39	12.47 ± 6.08	8.11 ± 2.06	0.15 ± 0.08	0.021	0.23 ± 0.08	0.0002

[a]Bonferroni adjustment p value.

dependent variable, the natural log transformation was applied to landmark error to normalize the data distribution.

The test of fixed effects from the fitted model shows a significant method×distance interaction (p value=0.006) which indicates that the mean difference in landmark error between methods varies with the initial distance. Thus, pairwise comparison of the SSTVD method with the SSD method and with the MI method was done at each distance interval. The tests for these pairwise comparisons were performed using test of mean contrast based on parameter estimates from the fitted model. Since multiple tests were performed, the p values for the pairwise comparisons were adjusted using Bonferroni's method to account for the number of tests performed (which are eight tests, two pairwise comparisons at four distances). The estimate of the mean landmark error for each method computed from the fitted linear mixed model and the mean ratio are shown in Table II. Landmark error for the SSTVD method compared to the SSD method is, on average, 69%+13% smaller at initial distances of $s<20$ mm and 74%+11% smaller at $20\leqslant s<40$ mm. Significantly smaller landmark error for the SSTVD method compared to the SSD method was observed at $40\leqslant s<60$ mm and $s\geqslant60$ mm, with the SSTVD method error being smaller by 83%+7% and 85%+8%, respectively.

Figure 3 shows an example of the distribution of landmark distances along the z axis (from apex to base) before and after registrations using both the SSTVD method and the SSD method. The initial landmark distance increases as landmarks are closer to the base [see Fig. 3(a)] since the deformation of the lung is mainly driven by the diaphragm. However, with the SSTVD method, the landmark distances decrease and all landmarks have an approximately uniform error distribution from apex to base in Fig. 3(b). This means that the SSTVD method shows good registration for both small and large deformations within the same lung independent of lung location. Also note in Fig. 3(b) that the landmarks have a large deviation of errors for the SSD method.

Figures 4(a) and 4(b) show surface distance maps of the warped TLC major vessel tree to the FRC major vessel tree for the SSTVD method and the SSD methods, respectively. The FRC major vessel tree is also shown in white for reference. The warped TLC major vessel tree is obtained by applying the transformation to the surface mesh of the TLC tree. Vessel trees at both TLC and FRC images are automatically extracted by using the algorithm of Shikata *et al.*[37] implemented in the Pulmonary Workstation (VIDA Diagnostics, Coralville, Iowa). The major vessel trees are then obtained by applying morphology opening with a structure element of $3\times3\times3$ voxels, followed by a connected component process on the segmented vessel trees to remove small branches. Figure 4(a) demonstrates that the surface distances are less than 2 mm for the SSTVD method. Large distances of some segments are possibly due to the inconsistent tree structure between TLC and FRC caused by segmentation or morphology operation steps. Examples are marked as A and B in Fig. 4(a), which show cases with missing segments in the FRC major trees. In contrast to the SSTVD, the SSD method yields an obvious mismatch in several re-

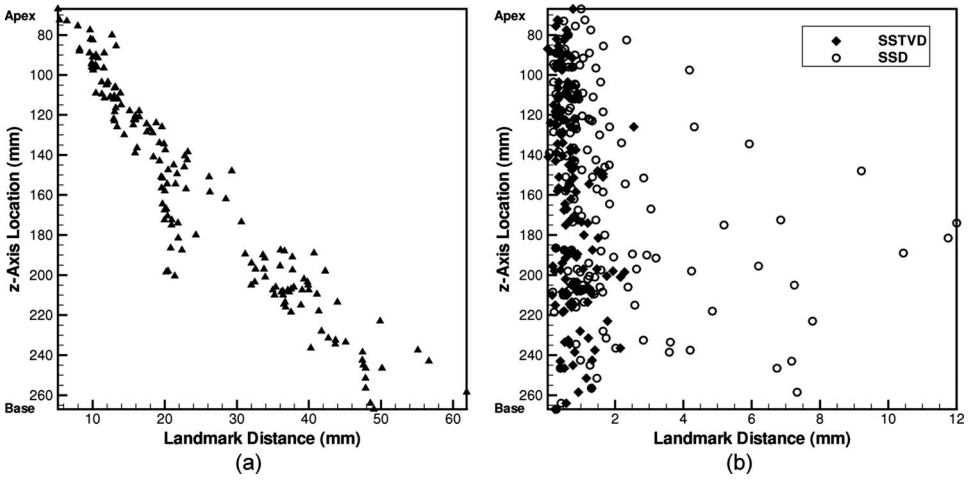

FIG. 3. Distribution of landmark distance along the z axis (from apex to base) (a) before and (b) after registrations using the SSTVD method (filled diamond) and the SSD method (unfilled circle) for registration pair A. Note that all landmarks have an approximately uniform error distribution from apex to base for the SSTVD method while they have a large deviation of error for the SSD method in (b).

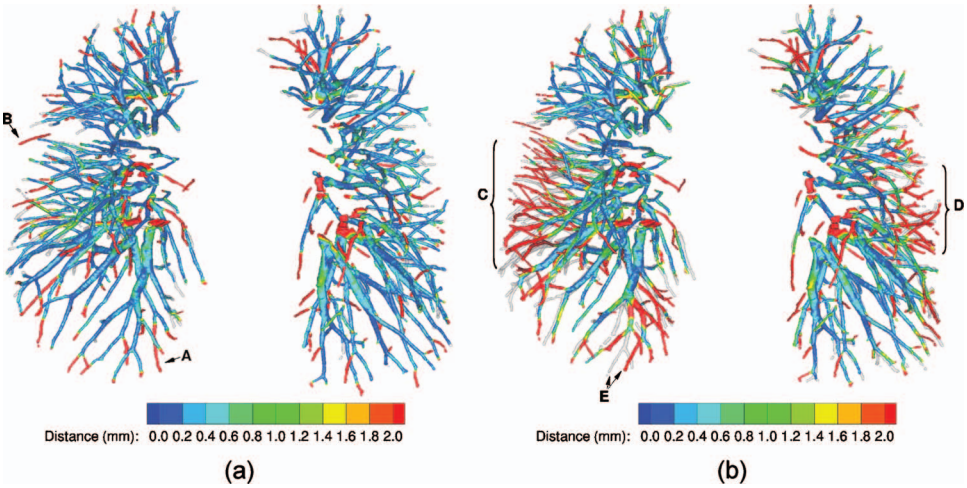

FIG. 4. Surface distance maps of the warped TLC major vessel tree to the FRC major vessel tree for the (a) SSTVD method and the (b) SSD method. The FRC major vessel tree is shown in white for reference. Note that the red segments in (a) are caused by missing segments in FRC major tree, not by mis-registration. Examples are marked as A and B. Segments with large errors in (b), marked as C, D, and E, are due to clear mis-registration, as one can easily see that the white unwarped segments misalign with the color coded tree.

gions, marked as C, D, and E in Fig. 4(b). One can see that the white unwarped segments misalign with the color coded tree in these regions.

Figures 5 and 6 show a slice from registration pairs A and F, respectively. These two registration pairs are chosen because one has the smallest lung volume difference and the other has the largest (see Table I) among all registration pairs tested here. In each figure, the slice from the reference image is shown in (a), the corresponding slice from the warped image obtained from the SSTVD method is shown in (b), and the corresponding slice from the warped image obtained from the SSD method is shown in (c). Although both methods yield a good alignment of the overall shapes of lungs, it can be seen that the SSTVD approach improves the alignment of structures within the lungs, such as the vessels and fissures.

The proposed SSTVD similarity measure is further compared to MI using the same statistical method described earlier for the SSTVD vs SSD comparison. For MI, we used a publicly available registration package elastix (http://elastix.isi.uu.nl/).[21,38,39] The optimal parameters specified in elastix include five levels of resolution for both the images and the transformation, a stochastic gradient descent optimization method[38] using a decaying function of the iteration number k: $a_k=a/(A+K)^{\alpha}$ with user-defined constants $A=50$ and $\alpha=0.6$. a was set to 50 000.0, 30 000.0, 10 000.0, 10 000.0, and 5000.0 for the five resolutions. The statistical comparisons of landmark errors between the SSTVD method and the MI method can be seen in Table II. Mean landmark error does not differ between the two methods at initial distances of $s<20$ mm, $20\leqslant s<40$ mm, and $40\leqslant s<60$ mm. At initial distances of $s\geqslant 60$ mm, the mean landmark error for the SSTVD method is 77%+8% smaller than the MI method (p value=0.0002). This is consistent with our hypothesis that the SSTVD provides registration improvements for large deformations such as occur when comparing TLC and FRC image datasets as done in this study.

IV. DISCUSSION

We have presented a nonrigid image registration method to align two CT lung datasets acquired during breath-holds at different lung volumes. Our method is of particular use when the volume differences between the two image sets are large as demonstrated in Table II, utilizing TLC and FRC scans. In order to take into consideration changes in the voxel intensity of lungs with inflation, we introduced the sum of squared tissue volume difference as the similarity criterion. This new criterion aims to minimize the local tissue volume difference within the lungs between matched regions. The local tissue volume difference is contributed by two factors: Change in the regional volume due to deformation and change in the fractional tissue content within a region due to respiration. The change in the regional volume is calculated from the

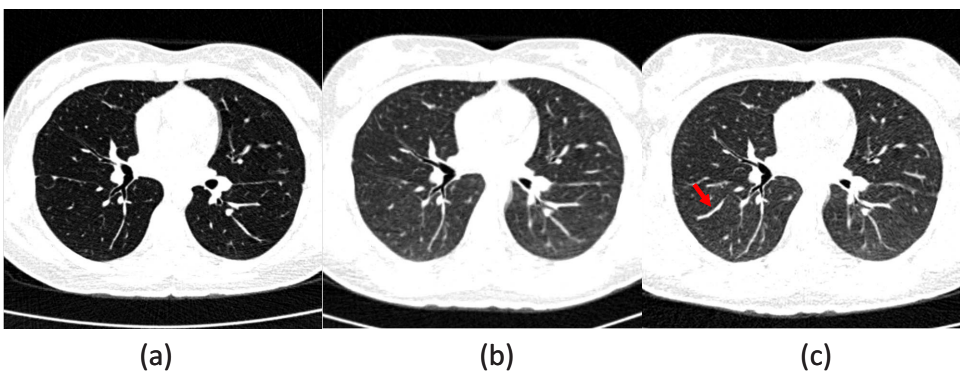

FIG. 5. A slice from the registration pair A. (a) Slice from the reference image. (b) Corresponding slice from the warped image with the SSTVD method. (c) Corresponding slice from the warped image with the SSD method. Notice a misalignment of vessel trees indicated by the arrow for the SSD method in (c).

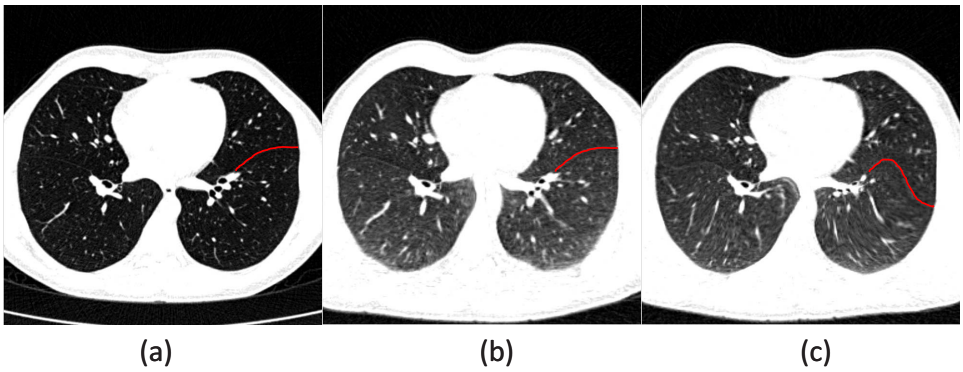

FIG. 6. A slice from the registration pair F. (a) Slice from the reference image. (b) Corresponding slice from the warped image with the SSTVD method. (c) Corresponding slice from the warped image with the SSD method. Notice the good alignment between the lobar fissures (highlighted in lines) and between the vessel trees for the SSTVD method in (b), while an obvious misalignment of the fissure and vessels for the SSD method in (c).

Jacobian value of the deformation and the change in the fractional tissue content is estimated from the HU. A composite of multilevel B-spline transformations is adopted and a sufficient condition is imposed to ensure a one-to-one transformation even for a pair of datasets with large volume differences.

To evaluate the effectiveness of the new similarity measure, we performed registrations for six lung volumetric pairs which were acquired at near TLC and FRC in the same scanning session. Over 100 landmarks located at vessel bifurcations were generated for each registration pair and the results show that the SSTVD method yields smaller average landmark errors than the SSD method. In addition, visual inspection shows that the SSTVD approach improves the alignment of structures within the lungs, although both the SSD and SSTVD methods give a good alignment of the overall shapes of lungs.

Recently, Gorbunova *et al.*[40] independently proposed a similar similarity criterion as our SSTVD to monitor disease progression in longitudinal image studies where volume differences are smaller than those used here and, with pathology progression, tissue densities can undergo considerable changes. Different from their work, we seek to apply this approach to match multiple lung volumes acquired between TLC and FRC in the same scanning session or over short periods of time with one goal trying to apply to computational fluid dynamics studies with moving lung boundaries.[41,42] The registrations are performed to match those datasets to adjust the geometry of airways for changes in lung volumes and to estimate the boundary condition by accounting for regional lung distensibility. In estimating the regional lung distensibility from a TLC-FRC registration pair, Yin *et al.*[43] demonstrated that the SSTVD method yields a much more physiologically consistent ventilation map than that of SSD. In this work, all datasets were from a well calibrated scanner, whereby imaged air is −1000 HU and water is 0. However, the SSTVD can be extended to the cases when the scanner is out of calibration. Imaged air and tissue can be sampled at the center of the trachea (air) and aorta (blood). Assuming that the HUs are linear between these ends of the scale, a voxel-by-voxel shift can be achieved. This is an important step as it is becoming well recognized that there are fairly significant variabilities between manufacturers in regard to the HUs of reconstructed air within the thorax.[22,44]

Currently, the total computational time on a single 3 GHz processor for one registration pair is nearly 4 h for the SSTVD method and is less than 1 h for the SSD method. The most time-consuming part for the SSTVD method is to calculate the Jacobian and the derivative of Jacobian with respect to the transformation parameter. The computation time increases dramatically as the image resolution increases since all voxels inside the masks are used during the registration. It takes less than 1 h for the first four registration levels, while it takes 3 h for the last two registration levels (the finest image resolution). Work is in progress to improve the computational efficiency of the SSTVD method by parallelization or the use of sample points instead of all voxels.[38]

ACKNOWLEDGMENTS

This work was supported in part by NIH Grant Nos. NIH-R01-HL-064368, NIH-R01-EB-005823, NIH-S10-RR-022421, and NIH-R01-HL-079406 and a University of Iowa CTSA NIH/NCRR Grant No. 1UL1RR024979. The authors would like to thank Dr. Joseph M. Reinhardt and Dr. Gary E. Christensen for their insightful suggestion, and Mr. Kai Ding for help in generating lung landmarks. They also thank Dr. Miriam Bridget Zimmerman for statistical consultation and Dr. Marius Starring for help in optimizing the elastix parameters for mutual information.

[a]Founder and shareholder of VIDA Diagnostics which is commercializing some of the software utilized in this work.
[b]Electronic mail: ching-long-lin@uiowa.edu

[1]W. R. Crum, T. Hartkens, and D. L. G. Hill, "Non-rigid image registration: Theory and practice," Br. J. Radiol. **77**, 140–153 (2004).
[2]B. Li, G. E. Christensen, E. A. Hoffman, G. McLennan, and J. M. Reinhardt, "Establishing a normative atlas of the human lung: Intersubject warping and registration of volumetric CT images," Acad. Radiol. **10**, 255–265 (2003).
[3]I. Sluimer, M. Prokop, and B. van Ginneken, "Towards automated segmentation of the pathological lung in CT," IEEE Trans. Med. Imaging **24**, 1025–1038 (2005).
[4]D. Sarrut, V. Boldea, S. Miguet, and C. Ginestet, "Simulation of four-dimensional CT images from deformable registration between inhale and exhale breath-hold CT scans," Med. Phys. **33**, 605–617 (2006).

[5]G. E. Christensen, J. H. Song, W. Lu, I. E. Naqa, and D. A. Low, "Tracking lung tissue motion and expansion/compression with inverse consistent image registration and spirometry," Med. Phys. **34**, 2155–2163 (2007).
[6]J. M. Reinhardt, K. Ding, K. Cao, G. E. Christensen, E. A. Hoffman, and S. V. Bodas, "Registration-based estimates of local lung tissue expansion compared to xenon CT measures of specific ventilation," Med. Image Anal. **12**, 752–763 (2008).
[7]T. Guerrero, K. Sanders, E. Castillo, Y. Zhang, L. Bidaut, T. Pan, and R. Komaki, "Dynamic ventilation imaging from four-dimensional computed tomography," Phys. Med. Biol. **51**, 777–791 (2006).
[8]M. Betke, H. Hong, D. Thomas, C. Prince, and J. P. Ko, "Landmark detection in the chest and registration of lung surfaces with an application to nodule registration," Med. Image Anal. **7**, 265–281 (2003).
[9]D. Paquin, D. Levy, and L. Xing, "Hybrid multiscale landmark and deformable image registration," Math. Biosci. Eng. **4**, 711–737 (2007).
[10]P. Li, U. Malsch, and R. Bendl, "Combination of intensity-based image registration with 3D simulation in radiation therapy," Phys. Med. Biol. **53**, 4621–4637 (2008).
[11]D. Sarrut, S. Delhay, P. Villard, V. Boldea, M. Beuve, and P. Clarysse, "A comparison framework for breathing motion estimation methods from 4-D imaging," IEEE Trans. Med. Imaging **26**, 1636–1648 (2007).
[12]R. Shekhar, P. Lei, C. Castro-Pareja, W. Plishker, and W. DSouza, "Automatic segmentation of phase-correlated CT scans through nonrigid image registration using geometrically regularized free-form deformation," Med. Phys. **34**, 3054–3066 (2007).
[13]B. Li, G. E. Christensen, G. McLennan, E. A. Hoffman, and J. M. Reinhardt, "Pulmonary CT image registration and warping for tracking tissue deformation during the respiratory cycle through 3-D consistent image registration," Med. Phys. **35**, 5575–5583 (2008).
[14]D. Yang, W. Lu, D. Low, J. Deasy, A. Hope, and I. El Naqa, "4D-CT motion estimation using deformable image registration and 5D respiratory motion modeling," Med. Phys. **35**, 4577–4590 (2008).
[15]D. A. Torigian, W. B. Gefter, J. D. Affuso, K. Emami, and L. Dougherty, "Application of an optical flow method to inspiratory and expiratory lung MDCT to assess regional air trapping: A feasibility study," AJR, Am. J. Roentgenol. **188**, W276–280 (2007).
[16]T. Guerrero, G. Zhang, T. Huang, and K. Lin, "Intrathoracic tumor motion estimation from CT imaging using the 3D optical flow method," Phys. Med. Biol. **49**, 4147–4161 (2004).
[17]L. Dougherty, J. C. Asmuth, and W. B. Gefter, "Alignment of CT lung volumes with an optical flow method," Acad. Radiol. **10**, 249–254 (2003).
[18]E. Schreibmann, G. Chen, and L. Xing, "Image interpolation in 4D CT using a BSpline deformable registration model," Int. J. Radiat. Oncol., Biol., Phys. **64**, 1537–1550 (2006).
[19]J. P. W. Pluim, J. B. A. Maintz, and M. A. Viergever, "Mutual-information-based registration of medical images: A survey," IEEE Trans. Med. Imaging **22**, 986–1004 (2003).
[20]M. M. Coselmon, J. M. Balter, D. L. McShan, and M. L. Kessler, "Mutual information based CT registration of the lung at exhale and inhale breathing states using thin-plate splines," Med. Phys. **31**, 2942–2948 (2004).
[21]M. Staring, S. Klein, and J. P. W. Pluim, "A rigidity penalty term for nonrigid registration," Med. Phys. **34**, 4098–4108 (2007).
[22]E. A. Hoffman, "Effect of body orientation on regional lung expansion: A computed tomographic approach," J. Appl. Physiol. **59**, 468–480 (1985).
[23]E. A. Hoffman *et al.*, "Characterization of the interstitial lung diseases via density-based and texture-based analysis of computed tomography images of lung structure and function," Acad. Radiol. **10**, 1104–1118 (2003).
[24]G. Christensen and H. Johnson, "Consistent image registration," IEEE Trans. Med. Imaging **20**, 568–582 (2001).
[25]T. Rohlfing, C. R. Maurer, D. A. Bluemke, and M. A. Jacobs, "Volume-preserving nonrigid registration of mr breast images using free-form deformation with an incompressibility constraint," IEEE Trans. Med. Imaging **22**, 730–741 (2003).
[26]D. Rueckert, L. I. Sonoda, C. Hayes, D. L. G. Hill, M. O. Leach, and D. J. Hawkes, "Nonrigid registration using free-form deformation: Application to breast MR images," IEEE Trans. Med. Imaging **18**, 712–721 (1999).
[27]J. Kybic and M. Unser, "Fast parametric elastic image registration," IEEE Trans. Med. Imaging **12**, 1427–1422 (2003).
[28]S. Lee, G. Wolberg, K. Y. Chwa, and S. Y. Shin, "Image metamorphosis with scattered feature constraints," IEEE Trans. Vis. Comput. Graph. **2**, 337–354 (1996).
[29]Y. Choi and S. Lee, "Injectivity conditions of 2D and 3D uniform cubic B-spline functions," Graphical Models **62**, 411–427 (2000).
[30]S. Lee, G. Wolberg, and S. Y. Shin, "Scatter data interpolation with multilevel B-spline," IEEE Trans. Vis. Comput. Graph. **3**, 1–17 (1997).
[31]D. Rueckert, P. Aljabar, R. A. Heckemann, J. V. Hajnal, and A. Hammers, "Diffeomorphic registration using B-splines," *MICCAI '06: Proceedings of the Ninth International Conference on Medical Image Computing and Computer-Assisted Intervention* (Springer, Berlin, 2006), pp. 702–709.
[32]M. K. Fuld, R. B. Easley, O. Saba, D. Chon, J. M. Reinhardt, E. A. Hoffman, and B. A. Simon, "CT measured regional specific volume change reflects regional specific ventilation in supine sheep," J. Appl. Physiol. **104**, 1177–1184 (2008).
[33]D. Mattes, D. R. Haynor, H. Vesselle, T. K. Lewellen, and W. Eubank, "PET-CT image registration in the chest using free-form deformations," IEEE Trans. Med. Imaging **22**, 120–128 (2003).
[34]R. H. Byrd, P. Lu, J. Nocedal, and C. Zhu, "A limited memory algorithm for bound constrained optimization," SIAM J. Sci. Comput. (USA) **16**, 1190–1208 (1995).
[35]S. Hu, E. A. Hoffman, and J. M. Reinhardt, "Automatic lung segmentation for accurate quantitation of volumetric x-ray CT images," IEEE Trans. Med. Imaging **20**, 490–498 (2001).
[36]K. Murphy, B. Ginneken, J. P. Pluim, S. Klein, and M. Staring, "Semi-automatic reference standard construction for quantitative evaluation of lung CT registration," *MICCAI '08: Proceedings of the 11th International Conference on Medical Image Computing and Computer-Assisted Intervention* (Springer, Berlin, 2008), pp. 1006–1013.
[37]H. Shikata, E. A. Hoffman, and M. Sonka, "Automated segmentation of pulmonary vascular tree from 3D CT images," *SPIE Medical Imaging '04* (SPIE, Bellingham, WA, 2004), Vol. 5369, pp. 107–116.
[38]S. Klein, M. Staring, and J. Pluim, "Evaluation of optimization methods for nonrigid medical image registration using mutual information and B-splines," IEEE Trans. Image Process. **16**, 2879–2890 (2007).
[39]S. Klein, M. Staring, and J. Pluim, "Nonrigid registration with tissue-dependent filtering of the deformation field," Phys. Med. Biol. **52**, 6879–6892 (2007).
[40]V. Gorbunova, P. Lo, H. Ashraf, A. Dirksen, M. Nielsen, and M. de Bruijne, "Weight preserving image registration for monitoring disease progression in lung CT," *MICCAI '08: Proceedings of the 11th International Conference on Medical Image Computing and Computer-Assisted Intervention* (Springer, Berlin, 2008), pp. 863–870.
[41]C.-L. Lin, M. H. Tawhai, G. McLennan, and E. A. Hoffman, "Multiscale simulation of gas flow in subject-specific models of the human lung," IEEE Eng. Med. Biol. Mag. **28**, 25–33 (2009).
[42]C.-L. Lin, M. H. Tawhai, G. McLennan, and E. A. Hoffman, "Characteristics of the turbulent laryngeal jet and its effect on airflow in the human intra-thoracic airways," Respir. Physiol. Neurbiol. **157**, 295–309 (2007).
[43]Y. Yin, E. A. Hoffman, and C.-L. Lin, "Local tissue-weight-based nonrigid registration of lung images with application to regional ventilation," *SPIE Medical Imaging '09* (SPIE, Bellingham, WA, 2009), Vol. 7262, p. 72620C.
[44]B. C. Stoel, F. Bode, A. Rames, S. Soliman, J. H. C. Reiber, and J. Stolk, "Quality control in longitudinal studies with computed tomographic densitometry of the lungs," Proc. Am. Thorac. Soc. **5**, 929–933 (2008).